

# Artificial water channels enable fast and selective water permeation through water-wire networks

Woochul Song<sup>1,10</sup>, Himanshu Joshi<sup>2</sup>, Ratul Chowdhury<sup>1</sup>, Joseph S. Najem<sup>3,11</sup>, Yue-xiao Shen<sup>4</sup>, Chao Lang<sup>1</sup>, Codey B. Henderson<sup>5</sup>, Yu-Ming Tu<sup>1,10</sup>, Megan Farrell<sup>1</sup>, Megan E. Pitz<sup>3</sup>, Costas D. Maranas<sup>1</sup>, Paul S. Cremer<sup>5</sup>, Robert J. Hickey<sup>6</sup>, Stephen A. Sarles<sup>3</sup>, Jun-li Hou<sup>7</sup>, Aleksei Aksimentiev<sup>1,2</sup> and Manish Kumar<sup>1,8,9,12\*</sup>

**Artificial water channels are synthetic molecules that aim to mimic the structural and functional features of biological water channels (aquaporins). Here we report on a cluster-forming organic nanoarchitecture, peptide-appended hybrid[4]arene (PAH[4]), as a new class of artificial water channels. Fluorescence experiments and simulations demonstrated that PAH[4]s can form, through lateral diffusion, clusters in lipid membranes that provide synergistic membrane-spanning paths for a rapid and selective water permeation through water-wire networks. Quantitative transport studies revealed that PAH[4]s can transport  $>10^9$  water molecules per second per molecule, which is comparable to aquaporin water channels. The performance of these channels exceeds the upper bound limit of current desalination membranes by a factor of  $\sim 10^4$ , as illustrated by the water/NaCl permeability-selectivity trade-off curve. PAH[4]s' unique properties of a high water/solute permselectivity via cooperative water-wire formation could usher in an alternative design paradigm for permeable membrane materials in separations, energy production and barrier applications.**

Aquaporins (AQPs) are cellular membrane proteins that mediate the translocation of water molecules across a physical membrane barrier at very high water permeation rates ( $>10^9$  H<sub>2</sub>O molecules per second per channel (H<sub>2</sub>O s<sup>-1</sup> channel<sup>-1</sup>) with an ultimate (theoretically infinite) water-to-ion selectivity to sustain the cellular homeostasis critical for maintaining life<sup>1,2</sup>. The unique structure and function of AQP-rich cell membranes, particularly their ideal water/salt permselectivity and spontaneous self-assembly and orientation in membrane matrices, are desirable features in desalination membranes<sup>3,4</sup>. Several attempts have been made to achieve a successful integration of AQPs into practical desalination membranes<sup>5</sup>. However, challenges with preserving the integrity and translating the function of the protein channels to larger scales during membrane fabrication processes have critically hampered researchers in achieving this goal<sup>6</sup>.

As alternatives to biological water channels, bioinspired artificial water channels (AWCs) have rapidly emerged as a promising platform for next-generation separation membranes<sup>7,8</sup>. AWCs are synthetic nanoarchitectures that mimic the function of AQPs. Insights from the wealth of structure–function relationships obtained from studies with AQPs have been used to suggest several biological channel traits as design criteria for AWCs, which include subnanometre unitary pore shape and a hydrophobic pore environment<sup>7,9</sup>. Recent successes in AWC integration into scalable polymeric membranes highlight their possible advantages over AQPs in terms of stability and high pore packing density<sup>10</sup>. Achieving both AQP-like

single channel water permeability and selectivity of AWCs, however, remains a challenge that limits the development of AWC-based desalination membranes<sup>10–16</sup>.

We report on a new class of unimolecular transmembrane AWCs, peptide-appended hybrid[4]arenes (PAH[4]s), which exhibit  $>10^9$  H<sub>2</sub>O s<sup>-1</sup> channel<sup>-1</sup> water permeability that is comparable to AQPs (Fig. 1a–d). This transport was achieved through channel cluster formation within the lipid bilayer membranes, which provided cooperatively enhanced membrane-spanning water permeation paths (Fig. 1e–j). The structural design of PAH[4] originated from our attempts to synthesize AWCs with a pore size of  $\sim 3$  Å (Supplementary Fig. 1), which is considered an ideal size for selective water permeation based on the pore geometries of AQPs<sup>17</sup>. However, transport studies revealed that PAH[4]s mediated water conduction through entirely different mechanisms to those of traditional channel configurations that possess one (for example, AQPs) or less than one (for example, gramicidin A) vertical permeation path per channel molecule<sup>18,19</sup>. PAH[4]s conducted water through a previously unreported mechanism owing to their unique structural and functional features (Fig. 1e,f).

## Rapid water permeation via channel cluster formation

PAH[4]s were synthesized by attaching eight D-L-D phenylalanine tripeptides (triPhe) chains on hybrid[4]arene macrocycle molecules (Fig. 1a, Supplementary Figs. 1–4 and Supplementary Video 1). Hybrid[4]arenes were employed as building templates

<sup>1</sup>Department of Chemical Engineering, The Pennsylvania State University, University Park, PA, USA. <sup>2</sup>Department of Physics, University of Illinois at Urbana-Champaign, Urbana, IL, USA. <sup>3</sup>Department of Mechanical, Aerospace, and Biomedical Engineering, The University of Tennessee, Knoxville, TN, USA. <sup>4</sup>Department of Civil, Environmental, & Construction Engineering, Texas Tech University, Lubbock, TX, USA. <sup>5</sup>Department of Chemistry, The Pennsylvania State University, University Park, PA, USA. <sup>6</sup>Department of Materials Science and Engineering, The Pennsylvania State University, University Park, PA, USA. <sup>7</sup>Department of Chemistry, Fudan University, Shanghai, China. <sup>8</sup>Department of Biomedical Engineering, The Pennsylvania State University, University Park, PA, USA. <sup>9</sup>Department of Civil and Environmental Engineering, The Pennsylvania State University, University Park, PA, USA. <sup>10</sup>Present address: Department of Chemical Engineering, The University of Texas at Austin, Austin, TX, USA. <sup>11</sup>Present address: Department of Mechanical Engineering, The Pennsylvania State University, University Park, PA, USA. <sup>12</sup>Present address: Department of Civil, Architectural and Environmental Engineering, The University of Texas at Austin, Austin, TX, USA. \*e-mail: [manish.kumar@utexas.edu](mailto:manish.kumar@utexas.edu)

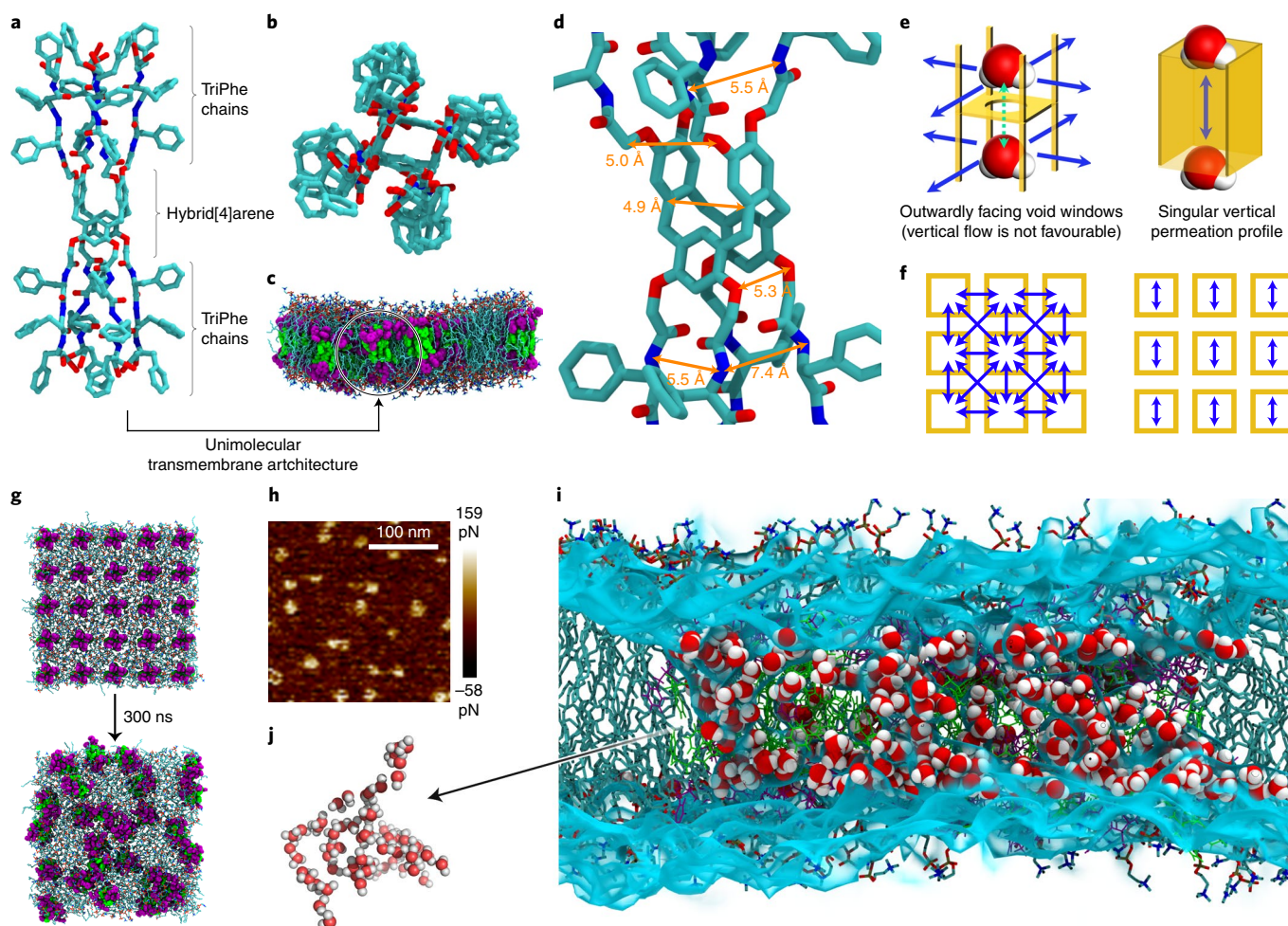


**Fig. 1 | Cluster-forming PAH[4] channels.** **a, b**, Side (**a**) and top (**b**) views of molecular models of PAH[4] indicate cylinder-like transmembrane structures. **c**, MD simulation snapshots of PAH[4]s that span lipid bilayer membranes. **d**, Tilted top view of energy-minimized PAH[4] structure shows outwardly facing void windows. **e, f**, Schematic comparison of the proposed water permeation paths (blue arrows) between PAH[4] (left) and traditional channel (right) configurations (**e**) and paths through nine channel aggregates (yellow boxes), seen from the top view, for PAH[4] (left) and traditional channel (right) configurations (**f**). **g**, Snapshots from an MD simulation showing lateral aggregation of PAH[4]s in lipid bilayer membrane patches. **h**, The AFM image (adhesion force) of PAH[4]-reconstituted supported lipid membranes shows aggregated domains of PAH[4] channels. **i**, Cross-sectional MD simulation snapshot of water permeation through a PAH[4] cluster embedded in a lipid bilayer patch, showing multiple water wires. **j**, A single illustrative water-wire network (of many) connecting the water compartments across the membrane. In the MD simulation panels, molecules are represented by the colours purple and green (PAH[4]), turquoise (lipid) and red and white (water).

primarily due to their desirable narrow internal cavity dimensions ( $\sim 3 \text{ \AA} \times \sim 5 \text{ \AA}$ ) for selective water permeation (Supplementary Fig. 1). The dynamic structure of PAH[4] within lipid bilayers, however, provided multiple water permeation paths that were preferred more than a single permeation path that vertically penetrates through each central cavity. As seen in the energy-minimized model of the PAH[4] molecule (Fig. 1d), triPhe chains are not rigidly held to each other by any specific interactions and form transient void windows that face outward with dimensions of around 5–7 Å, which are sterically and energetically more favourable for water permeation than the central pore cavity (Supplementary Fig. 5). This dynamic structure resulted in some interesting outcomes. When PAH[4]s clustered with each other within membranes, each void window could be interconnected with others from neighbouring channels to provide cooperatively interconnected membrane-spanning paths for water permeation through water-wire networks (Fig. 1e–j).

We investigated the water permeability of PAH[4]s in lipid bilayer membranes using stopped-flow light-scattering experiments. PAH[4]s were reconstituted into phosphatidylcholine/phosphatidylserine

(PC/PS) lipid vesicles ( $\sim 200 \text{ nm}$  in diameter) with different molar ratios of channels to lipids (mCLRs) and the vesicles were exposed to outwardly directed osmotic pressure gradients (shrinking mode of the vesicles). The water efflux from vesicles driven by osmotic pressure was evaluated by monitoring the scattering-intensity change of the vesicles, as was done in several recent studies (Supplementary Fig. 6)<sup>9,13,14</sup>. The rapid kinetics seen in the scattering traces indicates a faster size change of vesicles with channel incorporation and, consequently, a higher vesicular membrane permeability. The water permeability of lipid membranes increased with increasing mCLRs, which indicates that the embedded PAH[4]s enhanced the membranes' water permeation rates (Fig. 2a and Supplementary Fig. 7). Single PAH[4] channel water permeability could be calculated by counting the actual number of PAH[4]s per unit membrane area obtained from fluorescence correlation spectroscopy (FCS) measurements (Supplementary Figs. 8 and 9) at different mCLRs<sup>9,10,13</sup>. Interestingly, PAH[4]s exhibited an enhanced single-channel permeability at higher channel densities ( $> \sim 700$  channels per square micrometre of lipid membrane area) and the single-channel

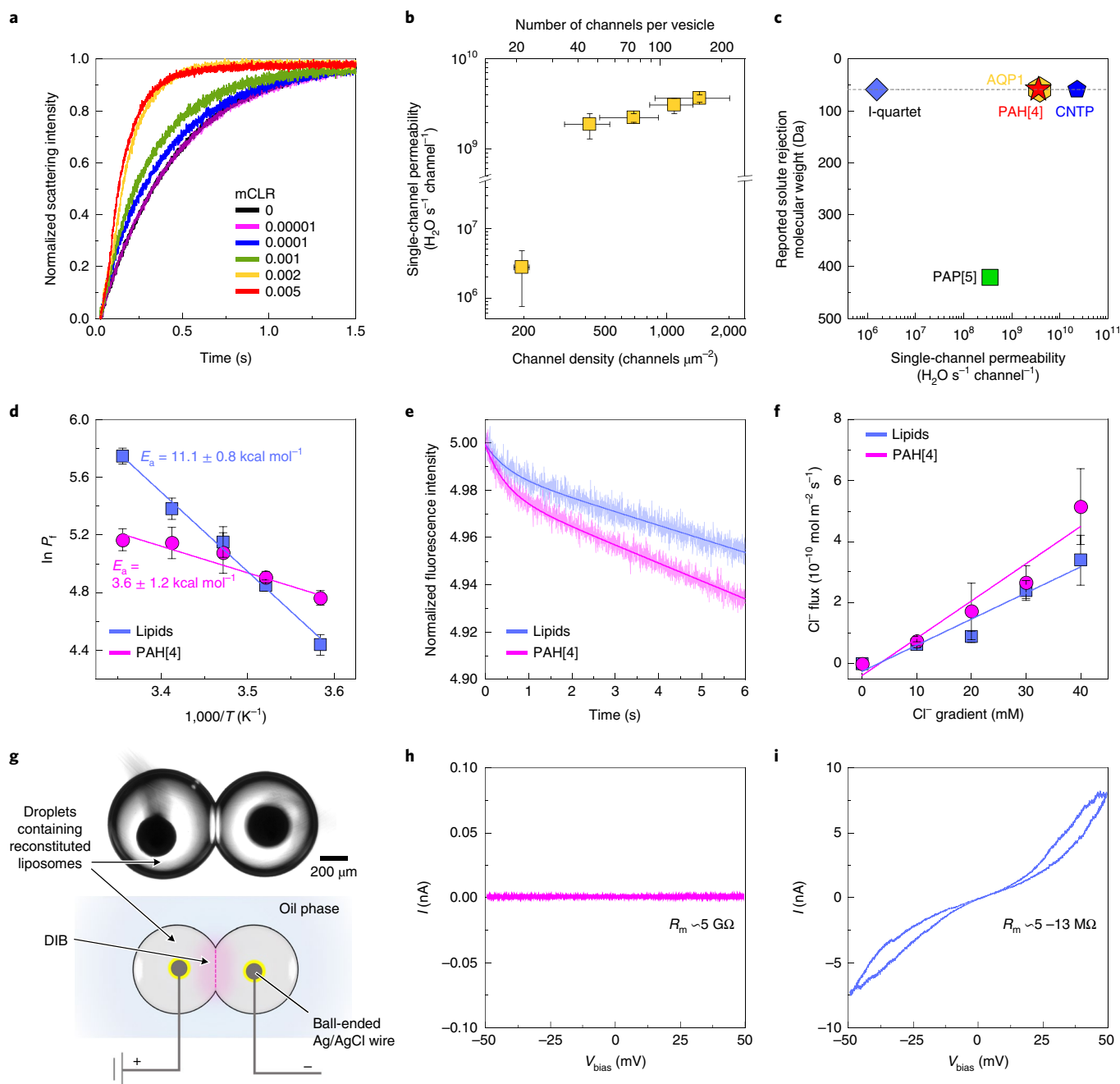


**Fig. 2 | Measurements of water and ion conduction rates through PAH[4]s.** **a**, Stopped-flow light scattering traces of PAH[4]-reconstituted PC/PS vesicles with different mCLRs under an inwardly directed osmotic gradient indicate an increasing permeability with increased channel concentrations. **b**, Single PAH[4] channel permeability measured at different channel densities indicates a jump in permeability when the channel concentrations reach a threshold between  $\sim 200$  channels  $\mu\text{m}^{-2}$  (or  $\sim 20$  channels per average sized vesicle) and  $\sim 420$  channels  $\mu\text{m}^{-2}$  (or  $\sim 45$  channels per vesicle), which suggests a possible cooperativity. **c**, Comparison of the calculated single channel permeability and the reported effective solute rejection property of representative artificial and biological water channels: imidazole quartet (I-quartet)<sup>11</sup>, PAP[5]<sup>12,13</sup>, AQP1 and CNTPs<sup>14</sup>. **d**, Arrhenius plots of the osmotic permeability ( $P_i$   $\mu\text{m}^2\text{s}^{-1}$ ) for the bare lipid membranes and the PAH[4]-mediated membrane permeability. **e**, Comparison of fluorescence intensity traces between the control and PAH[4]-reconstituted (mCLR 0.005) lipid vesicles that encapsulate lucigenin, measured in the presence of a 20 mM  $\text{Cl}^-$  concentration gradient. **f**, Plots of  $\text{Cl}^-$  flux as a function of  $\text{Cl}^-$  concentration (mM) gradients for both control and PAH[4]-reconstituted lipid membranes. **g**, Optical microscope image of hanging droplets with DIB at the droplet-contacting interface (top) and schematic illustration of the ionic current measurement set up (bottom). **h, i**,  $I$ - $V$  plots of PAH[4] (mCLR 0.005) (**h**) and PAP[5] (mCLR 0.002) (**i**) reconstituted membranes measured under the DIB system. The non-linearity of the  $I$ - $V$  curves of PAP[5] membranes is caused by the membrane area change due to electrowetting, not to the channels<sup>29,32</sup>.

permeability reached up to  $(3.7 \pm 0.3) \times 10^9 \text{H}_2\text{O s}^{-1} \text{channel}^{-1}$  or  $(1.1 \pm 0.1) \times 10^{-13} \text{cm}^3 \text{s}^{-1} \text{channel}^{-1}$  at 25 °C (Fig. 2b), the highest among the reported values of AWCs except for carbon nanotube porins (CNTPs) of  $\sim 8$  Å diameter. These values are even comparable

to that of aquaporin-1 (AQP1) ( $4.0 \times 10^9 \text{H}_2\text{O s}^{-1} \text{channel}^{-1}$ ) (Fig. 2c). Although we exploited most the widely adapted model to calculate water permeability of the PAH[4] channel to maintain a consistency of evaluating PAH[4] channels with published references, Pohl and

co-workers recently proposed a more accurate equation to quantify water permeability<sup>9,20</sup>. When this model was used for PAH[4]s, the single-channel permeability was calculated to be slightly lower at  $(8.9 \pm 0.8) \times 10^8 \text{ H}_2\text{O s}^{-1} \text{ channel}^{-1}$  (Supplementary Information gives details). It has been reported that the permeability of a specific AWC, peptide-appended pillar[5]arene (PAP[5]), was different in liposomes based on whether the permeability was measured in the swelling or the shrinkage mode<sup>12,13</sup>. However, only a small permeability enhancement (1.3–2.5 times) was observed for PAH[4] channels when measured in the swelling mode (Supplementary Fig. 10). It has also been reported that chaotropic osmolytes, such as poly(ethylene glycol), could disrupt intermolecular hydrogen bonds between water molecules and enhance the water permeation rate through CNTPs<sup>14</sup>, but this effect of osmolytes was not observed in the case of PAH[4] channels (Supplementary Fig. 11).

PAH[4] clusters in the lipid bilayer membranes were observed by atomic force microscopy (AFM) performed in an aqueous buffer (Fig. 1h) and the domain size of the channel clusters observed from AFM experiments match well with the number of PAH[4] subunits per vesicle estimated by FCS (Supplementary Fig. 12). Further, the cluster-forming behaviour of PAH[4]s in lipid bilayer membranes was confirmed via fluorescence recovery after photobleaching (FRAP) experiments (Supplementary Fig. 13) and molecular dynamics (MD) simulations (Fig. 1g). These results are similar to our recent study that demonstrated the aggregation behaviour of another triPhe chain-based unimolecular AWC, PAP[5]<sup>10,12,13</sup>. Combined with the increased single-channel permeability observed with increasing channel densities in the low membrane concentration range (Fig. 2b), these results indicate a cooperatively enhanced water permeation via channel cluster formation.

The measured single-channel permeability indicated that PAH[4]s can mediate water transport as efficiently as AQP1. This was further confirmed by measurement of the activation energy of water permeation through the channels (Fig. 2d and Supplementary Fig. 14). Control lipid membranes were shown to have an activation energy of  $11.1 \pm 0.8 \text{ kcal mol}^{-1}$  for water permeation, which corresponds to reported reference values of lipid bilayers in which water permeation takes place through the solution-diffusion mechanism<sup>21,22</sup>. The activation energy for PAH[4]-mediated water permeation was measured as  $3.6 \pm 1.2 \text{ kcal mol}^{-1}$ , which indicates a lower energy barrier for water permeation across the membranes by PAH[4] insertion. This low activation energy ( $<5 \text{ kcal mol}^{-1}$ ) is strong evidence of single-file water transport<sup>23</sup>. Based on the measured activation energy and the presumption of single-file water conduction, the permeability was calculated as  $6.9 \times 10^{-13} \text{ cm}^3 \text{ channel}^{-1}$ , which is in good agreement with the measured single PAH[4] permeability (Supplementary Information gives the calculation details). This confirms the single-file water permeation through PAH[4] architectures across the membranes<sup>23</sup>, which is also validated by our MD simulation results.

### Quantitative measurement of monovalent ion permeability

As mentioned above, to achieve both a high permeability and selectivity is a significant challenge for membrane systems in general and AWC systems in particular—the other challenge is methodological. The water-over-ion selectivity properties of all the AWCs reported so far have been obtained using qualitative techniques rather than numerical values, such as number ratios between permeating water and ion molecules, which represent intrinsic molecular transport properties<sup>16,24</sup>. This challenge was also recently discussed for desalination membranes and, to provide a baseline for membrane material development efforts, Park and co-workers reported an upper-bound plot of the intrinsic water/NaCl permeability–selectivity trade-off for representative polymeric desalination membranes<sup>25</sup>. We propose that to obtain the intrinsic transport properties of the channels is

quite important to achieve coherence in terms of evaluating AWCs for any future applications, including desalination.

A combination of colloidal quenching halide ion sensitive dyes (lucigenin dyes), stopped-flow fluorescence spectrometry and FCS techniques was exploited to evaluate the quantitative PAH[4] channel chloride ( $\text{Cl}^-$ ) permeability (Fig. 2e,f and Supplementary Fig. 15; Supplementary Information gives the analysis details).  $\text{Cl}^-$  ion fluxes were measured at different  $\text{Cl}^-$  concentration gradients for both the control and PAH[4]-reconstituted membranes (Fig. 2f and Supplementary Fig. 16) and the  $\text{Cl}^-$  permeability coefficient of lipid membranes was measured as  $(8.6 \pm 1.9) \times 10^{-10} \text{ cm s}^{-1}$ , which corresponds to the reported  $\text{Cl}^-$  permeability coefficients of lipid bilayers ( $10^{-8}$ – $10^{-11} \text{ cm s}^{-1}$ ) (ref. 26). The single PAH[4]  $\text{Cl}^-$  permeability was calculated using channel numbers per membrane area, obtained from the FCS analysis to be  $(9.5 \pm 3.6) \times 10^{-23} \text{ cm}^3 \text{ s}^{-1}$ . The channel area ( $\sim 2 \text{ nm}^2$ ) normalized  $\text{Cl}^-$  permeability coefficient was  $(4.7 \pm 1.7) \times 10^{-9} \text{ cm s}^{-1}$ , which is about fivefold higher than that of highly retentive lipid membranes. When combined with a water permeability of  $((3.6 \pm 0.3) \times 10^9 \text{ H}_2\text{O s}^{-1} \text{ channel}^{-1}$  or  $(1.1 \pm 0.1) \times 10^{-13} \text{ cm}^3 \text{ s}^{-1}$ ), PAH[4] exhibited an  $\sim 10^9$  water/salt selectivity that far surpasses the selectivity requirements ( $\sim 16,000$ ) for desalination membranes<sup>3</sup>.

The absence of suitably sensitive cation colloidal quenching dyes makes it difficult to measure the single-channel  $\text{Na}^+$  permeability. As an alternative, an assay based on 8-hydroxypyrene-1,3,6-trisulfonic acid dye was performed to observe if any effective  $\text{Na}^+$  permeation occurs through PAH[4]s, as this method has been widely adopted to test ion permeation through various ion channels<sup>27</sup>, but no detectable  $\text{Na}^+$  permeation was observed for PAH[4]-reconstituted membranes (Supplementary Fig. 17).

Ionic current measurements across PAH[4]-reconstituted lipid bilayers were performed to demonstrate the highly retentive ion permeation properties of PAH[4]s, using a droplet interface bilayer (DIB) system<sup>28,29</sup>. The DIB system exploits PAH[4]-reconstituted PC/PC vesicles, which were confirmed to have PAH[4]s embedded in membranes from the stopped-flow experiments, to form bilayers at the interface of two droplets and, thereby, maximize the opportunity of PAH[4] presence in the DIB membranes during the ionic current measurements (Fig. 2g and Supplementary Fig. 18). During the course of the current–voltage ( $I$ – $V$ ) measurements, PAH[4]-reconstituted membranes did not show any ionic current at any tested conditions and the resistance value of the membranes ( $R_m$ ,  $\sim 5 \text{ G}\Omega$ ) was equivalent to that of the control insulating lipid bilayer membranes<sup>28,30–32</sup>, which demonstrates the highly efficient ionic rejection of PAH[4]s (Fig. 2h). In terms of interpretation of this result, it is still possible that PAH[4]s were not successfully integrated into the membranes during the DIB formation process (Supplementary Fig. 18). Therefore, the unimolecular AWC PAP[5], which is structurally analogous to PAH[4] (Supplementary Fig. 2) and found to allow ion permeation in our previous study<sup>12,13</sup>, was used as a positive control and subjected to  $I$ – $V$  measurements using the DIB system to show the stable insertion of triPhe-chain-based unimolecular transmembrane structures into the membranes during the DIB formation. Under the same conditions, PAP[5]-reconstituted membranes showed significant ionic currents with lowered membrane resistance values of  $\sim 5$ – $13 \text{ M}\Omega$  (Fig. 2i).

### Evaluation of PAH[4] water-to-salt permselectivity

Based on experimentally measured molecular transport rates, the PAH[4] intrinsic permeabilities of water ( $P_w$ ) and salt ( $\text{NaCl}$  ( $P_s$ )) were calculated as  $(2.2 \pm 0.2) \times 10^{-6} \text{ cm}^2 \text{ s}^{-1}$  and  $(1.9 \pm 0.7) \times 10^{-15} \text{ cm}^2 \text{ s}^{-1}$ , respectively (Supplementary Information gives the analysis details), using chloride as the limiting ion. Note that, instead of the pore area, the cross-sectional channel area ( $\sim 2 \text{ nm}^2$ ) occupied in the membranes was used to calculate individual permeability values to provide a membrane engineering perspective<sup>33</sup>. As the water

channel integration efficiency into a biomimetic membrane matrix is another critical factor in evaluating channel-based membranes,  $P_w$  and  $P_s$  values for PAH[4]-reconstituted PC/PS lipid membranes were calculated for several cases of channel integration efficiency ( $\alpha$ ) that ranged from 0.01 to 1, and compared to reported desalination membranes' values (Fig. 3). Additionally, representative membranes based on biomimetic water channels (CNTPs and *Rhodobacter sphaeroides* aquaporin Z (RsAqpZ), which is reported to have the highest permeability among the AQP family<sup>34</sup>) were plotted using the same method to provide a comparison of the various types of channel-based biomimetic membranes possible for the development of desalination membranes. As shown in Fig. 3, the plot of water/salt selectivity ( $P_w/P_s$ ) against water permeability ( $P_w$ ) shows that PC/PS lipid membrane matrices by themselves are below the trade-off upper limit of polymeric desalination membranes. This is reasonable, given that water and salt permeations take place via the solution-diffusion mechanism for both cases. Remarkably, with a gradual increase in channel insertion into the membranes ( $\alpha \sim 0.01-1$ ), channel-based biomimetic membranes demonstrate water/NaCl selectivity that far exceeds state-of-the-art polymeric membranes' upper bound limit by several orders of magnitude (Fig. 3). We propose that this is a conservative estimate of the permeability-selectivity trend for PAH[4]-enhanced biomimetic matrices because we used quantitative  $\text{Cl}^-$  ion permeability as a model for NaCl permeability. Usually, under reverse-osmosis conditions,  $\text{Cl}^-$  permeation is limited by the slower diffusing  $\text{Na}^+$ . This assumption that  $\text{Na}^+$  is the limiting ion was used recently to estimate, based on indirect measurements, that biomimetic membranes could have NaCl selectivity in a range three orders of magnitude higher than that shown here<sup>33</sup>. Hence, values reported here represent the most conservative evaluation of PAH[4] channel-based desalination membranes with direct measurements of the channel transport rates. However, it is possible that PAH[4] channels could demonstrate an  $\sim 10^{12}$  water-to-salt selectivity as estimated in the previous study for AQPs<sup>33</sup> if  $\text{Na}^+$  ion transport rates could be measured accurately and used instead.

### Computer simulations of PAH[4] permeability

To provide detailed descriptions that relate the microstructure-to-molecular transport properties of PAH[4] clusters, representative PAH[4] cluster configurations were generated in silico<sup>35,36</sup> and subjected to MD simulations ( $\sim 400$  ns) in lipid bilayer patches (Fig. 4a,b and Supplementary Video 2) (Supplementary Information gives a detailed simulation analysis). As the PAH[4] configurations evolved from the monomer to the dimer and to 22-mer clusters, water permeability per PAH[4] molecule enhanced significantly, which suggests a cooperative water-permeating path formation between the PAH[4] molecules (Supplementary Figs. 19–26). The agreement in permeability values between experiment and simulation along with recapitulating the experimental trend of increasing permeability when clusters are formed with increasing channel density represents the appropriateness of the simulation setting to emulate oligomerized PAH[4] clusters in lipid membranes. In another set of simulations, a transmembrane voltage of  $\pm 1$  V was applied in two MD simulations of the PAH[4] 22-mer clusters that were most water conductive to measure the ionic conductance, but no ion permeation was observed during each 100 ns simulation, which confirms the ion-exclusion property of PAH[4] channels (Supplementary Video 3). In terms of a numerical value, these simulations indicate that the conductance of the membrane patch was  $< 1$  pS.

Full MD trajectories provided several insights into the rapid water permeation through PAH[4] clusters. First, all the permeating water molecules have to undergo at least one 'bulk-2D wire-bulk' transition. Two-dimensional water-wire formation is a crucial factor to enable a rapid water conduction via an almost perfect slippage of the water molecules, which cannot be achieved in the systems

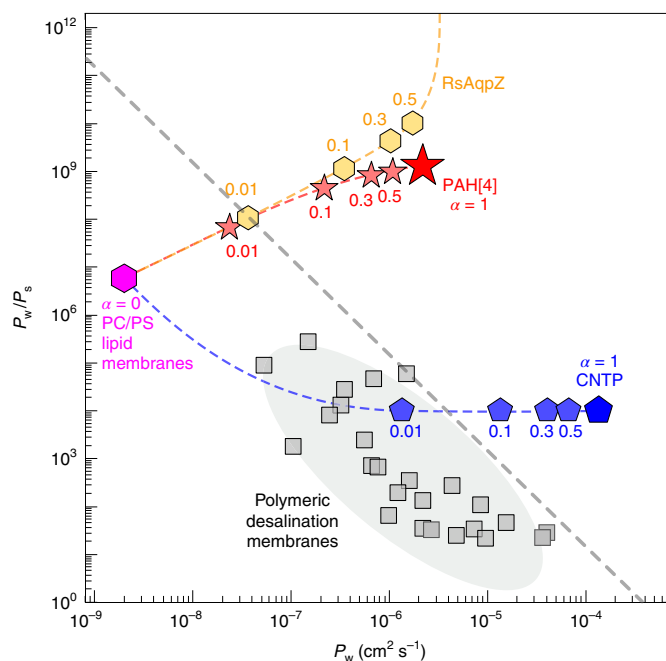


**Fig. 3 | Intrinsic water/NaCl selectivity ( $P_w/P_s$ ) versus  $P_w$  of PAH[4]-, CNTP- and RsAqpZ-based biomimetic membranes.** The data points of channel-reconstituted biomimetic membranes with PC/PS matrix molecules with an increasing fractional area of the membranes occupied by the channels ( $\alpha = 0.5$  indicates that 50% of membrane area is occupied by channels) are compared;  $\alpha$  values indicate the corresponding data points for the PAH[4] (red stars), RsAqpZ (orange hexagons) and CNTP (blue pentagons) membranes. The dashed lines for the channel-based membranes are guides for the eye. Data for the representative polymeric desalination membranes (grey squares) and their upper bound trade-off line (dashed grey line) are adapted from Geise et al.<sup>25</sup>.

in which continuum hydrodynamics is predominant<sup>37</sup>. Water-wire formation is not seen in monomeric PAH[4] configurations, which supports the assertion that PAH[4]s provide synergistic paths via cluster formation (Supplementary Fig. 27). Specifically, analyses of the number of hydrogen bonds for each of the  $\sim 800$  water molecules that permeated through the PAH[4] 22-mer cluster showed several interesting features in comparison to that in an AQP1 tetramer. As a water molecule approaches the centre of the membrane, the number of hydrogen bonds that it forms gradually reduces from an average of  $\sim 3.5$  to  $\sim 2.5$  on both sides of the membrane and then drops rapidly to  $\sim 1.5$  within the constriction region of the channel, at Z-axis values within  $9 \text{ \AA}$  of the membrane's midplane (Fig. 4c); the number of hydrogen bonds lower than two in the constriction region indicates that water molecules lose their bulk state, which enables a fast permeation in this region<sup>14</sup>. A similar dependence was observed for AQP1, with one major difference: the location of the minimally hydrogen-bonded water molecule was well-defined by the channel's structure, whereas this location was not well-defined in the dynamic PAH[4] clusters. Further, the varying numbers of hydrogen bonds formed by ten randomly chosen water molecules as they pass through each channel was plotted (Supplementary Fig. 28) for both the PAH[4] and AQP1 channels. This analysis indicated that, in the case of the PAH[4] cluster system, the number of hydrogen bonds of each water molecule could drop even lower than 1.5 during individual permeation events similar to that in AQP1 (Supplementary Fig. 28). However, owing to the lack of a well-defined structure for PAH[4] clusters, averaging over all the permeating molecule produces a slightly higher minimum number of

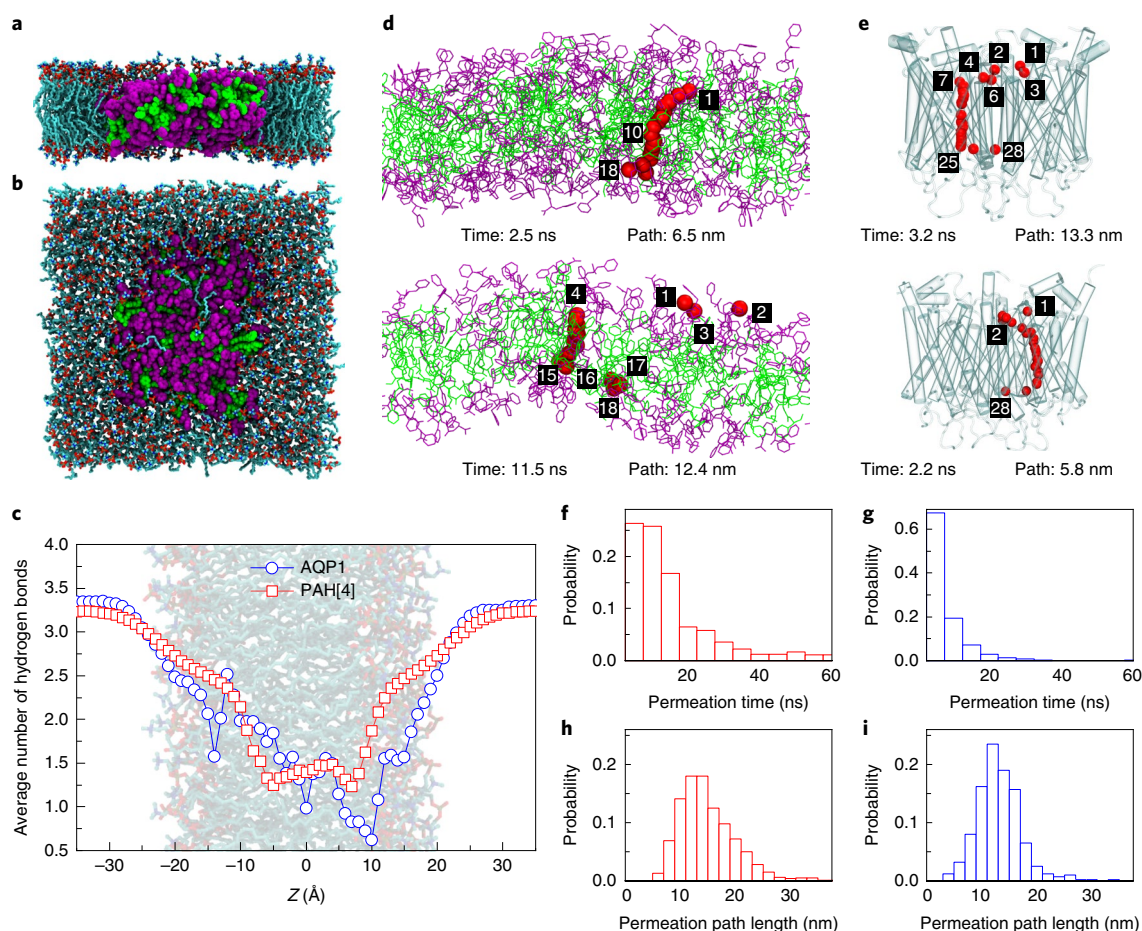


**Fig. 4 | MD simulations of a 22-mer cluster of PAH[4] channels and of an AQP1 tetramer embedded in a lipid bilayer membrane. a,b**, Side (a) and top (b) views of a PAH[4] 22-mer cluster (purple and green) embedded in a lipid bilayer membrane (turquoise); water and ions are not shown for clarity. **c**, Average number of hydrogen bonds formed by a permeating water molecule as a function of its Z coordinate in an AQP1 tetramer and a cluster of PAH[4] channels embedded in a lipid bilayer membrane. To calculate the number of hydrogen bonds, a 3.5 Å distance cutoff between the donor and acceptor and a 40° angle cutoff for the donor-hydrogen-acceptor angle were used. The number of hydrogen bonds was averaged over all the permeated water molecules during the course of the MD trajectory (~800 and ~400 for PAH[4] and AQP1, respectively). **d,e**, The approximated path of the two representative water molecules permeated through the PAH[4] cluster (d) and the AQP1 tetramer (e). The PAH[4] molecules are shown using green and purple lines, whereas the AQP1 channel is shown using white semi-transparent cylinders. The red spheres show the average location of the permeating water molecule in each 1 Å bin along the Z direction during the permeation path. Lipid and other water molecules are not shown for clarity. The numbers specify the bin index along the Z axis, from 1 to 18 or 1 to 28 bins for PAH[4] and AQP1, respectively; some bin numbers are omitted for clarity. The permeation path length and the permeation time of the respective water molecules are specified in each figure. **f,g**, The normalized distribution of the permeation time for all the water molecules that passed through the PAH[4] cluster (f) and the AQP1 tetramer (g). **h,i**, The normalized distribution of the permeation length for all the water molecules that passed through the PAH[4] cluster (h) and the AQP1 tetramer (i).

hydrogen bonds in the constriction region for PAH[4] as compared to that of AQP1.

We used the obtained dependence of the number of hydrogen bonds along the Z axis to define the average location of the channel constriction region for both the PAH[4] and AQP1 systems: (−9 Å, 9 Å) and (−14 Å, 14 Å), respectively. Having defined the boundaries of the channel constriction, we determined the path each water molecule took to permeate the PAH[4] cluster or the AQP1 tetramer (two such paths are shown for each system in Fig. 4d,e) and computed the time it took for each water molecule to pass from one side of the constriction to the other for both systems (Supplementary Fig. 29). The histograms of the normalized probability of the permeation times are shown in Fig. 4f,g for PAH[4] and AQP1, respectively. As expected, the histogram has a longer tail in the case of the PAH[4] 22-mer cluster, reflective of the more convoluted permeation path for some water molecules. The average permeation

time is, however, of the same order: 20.3 ns for PAH[4] and 5.5 ns for AQP1, with the AQP1 channel showing a fourfold faster transport per permeation path.

We further computed the average distance travelled by a water molecule (Supplementary Fig. 30). The average permeation path is slightly longer for the PAH[4] channel than that for AQP1, as can be seen from the normalized distributions of the water permeation path lengths (Fig. 4h,i). We used the average location of the water molecules in 1 Å Z-axis bins to visualize a typical permeation path through the PAH[4] cluster and AQP1 (Fig. 4d,e). In the case of AQP1, the permeation path is well-defined, whereas for PAH[4] the path can be either well-defined or dispersed. The results of our analysis suggest that both the average time and the average path taken by a water molecule that permeates through an PAH[4] cluster is of the same order as that for the AQP1 channel. Although both the permeation time and permeation path are statistically longer for

PAH[4], the overall permeation rate can approach that of AQP1 if a sufficient number of such channels simultaneously forms per unit area of the membrane, which provides highly efficient water permeation networks (Supplementary Videos 4 and 5). This conclusion is also supported by corresponding experimental observations (channel aggregation and increasing channel permeability at higher channel densities).

### Summary

The transmembrane unimolecular PAH[4] architecture was shown to enable a highly efficient and selective water permeation through mechanisms distinct from traditional water channels. These mechanisms include lateral aggregation and the formation of an interconnected water-wire network in a biomimetic membrane matrix, which results in intrinsic water/NaCl transport properties that exceed the permselectivity performance of the current desalination membranes by orders of magnitude. Combined with recent progress in maximizing the AWC insertion efficiency in bioinspired block copolymer membranes by up to ~60% and utilizing them for the fabrication of scalable membranes<sup>10</sup>, cluster-forming AWCs could pave the way for a unique architecture of bioinspired membranes for a variety of applications.

### Online content

Any methods, additional references, Nature Research reporting summaries, source data, extended data, supplementary information, acknowledgements, peer review information; details of author contributions and competing interests; and statements of data and code availability are available at <https://doi.org/10.1038/s41565-019-0586-8>.

Received: 11 May 2019; Accepted: 4 November 2019;

Published online: 16 December 2019

### References

- Preston, G. M., Carroll, T. P., Guggino, W. B. & Agre, P. Appearance of water channels in xenopus oocytes expressing red cell CHIP28 protein. *Science* **256**, 385–387 (1992).
- Noda, Y., Sohara, E., Ohta, E. & Sasaki, S. Aquaporins in kidney pathophysiology. *Nat. Rev. Nephrol.* **6**, 168 (2010).
- Park, H. B., Kamcev, J., Robeson, L. M., Elimelech, M. & Freeman, B. D. Maximizing the right stuff: the trade-off between membrane permeability and selectivity. *Science* **356**, eaab0530 (2017).
- Werber, J. R., Osuji, C. O. & Elimelech, M. Materials for next-generation desalination and water purification membranes. *Nat. Rev. Mater.* **1**, 16018 (2016).
- Shen, Y.-x., Saboe, P. O., Sines, I. T., Erbakan, M. & Kumar, M. Biomimetic membranes: a review. *J. Membr. Sci.* **454**, 359–381 (2014).
- Hélix-Nielsen, C. Biomimetic membranes as a technology platform: challenges and opportunities. *Membranes* **8**, 44 (2018).
- Song, W., Lang, C., Shen, Y.-x. & Kumar, M. Design considerations for artificial water channel-based membranes. *Ann. Rev. Mater. Res.* **48**, 57–82 (2018).
- Song, W., Tu, Y.-M., Oh, H., Samineni, L. & Kumar, M. Hierarchical optimization of high-performance biomimetic and bioinspired membranes. *Langmuir* **35**, 589–607 (2019).
- Horner, A. et al. The mobility of single-file water molecules is governed by the number of H-bonds they may form with channel-lining residues. *Sci. Adv.* **1**, e1400083 (2015).
- Shen, Y.-x. et al. Achieving high permeability and enhanced selectivity for angstrom-scale separations using artificial water channel membranes. *Nat. Commun.* **9**, 2294 (2018).
- Licsandru, E. et al. Salt-Excluding artificial water channels exhibiting enhanced dipolar water and proton translocation. *J. Am. Chem. Soc.* **138**, 5403–5409 (2016).
- Chen, L. et al. Chiral selective transmembrane transport of amino acids through artificial channels. *J. Am. Chem. Soc.* **135**, 2152–2155 (2013).
- Shen, Y.-x. et al. Highly permeable artificial water channels that can self-assemble into two-dimensional arrays. *Proc. Natl Acad. Sci. USA* **112**, 9810–9815 (2015).
- Tunuguntla, R. H. et al. Enhanced water permeability and tunable ion selectivity in subnanometer carbon nanotube porins. *Science* **357**, 792–796 (2017).
- Freger, V. Selectivity and polarization in water channel membranes: lessons learned from polymeric membranes and CNTs. *Faraday Discuss.* **209**, 371–388 (2018).
- Song, W. & Kumar, M. Artificial water channels: toward and beyond desalination. *Curr. Opin. Chem. Eng.* **25**, 9–17 (2019).
- Sui, H., Han, B.-G., Lee, J. K., Walian, P. & Jap, B. K. Structural basis of water-specific transport through the AQP1 water channel. *Nature* **414**, 872–878 (2001).
- Tajkhorshid, E. et al. Control of the selectivity of the aquaporin water channel family by global orientational tuning. *Science* **296**, 525–530 (2002).
- Saparov, S. M. et al. Mobility of a one-dimensional confined file of water molecules as a function of file length. *Phys. Rev. Lett.* **96**, 148101 (2006).
- Hanneschläger, C., Barta, T., Siligan, C. & Horner, A. Quantification of water flux in vesicular systems. *Sci. Rep.* **8**, 8516 (2018).
- Borgnia, M. J., Kozono, D., Calamita, G., Maloney, P. C. & Agre, P. Functional reconstitution and characterization of AqpZ, the *E. coli* water channel protein11 edited by W. Baumeister. *J. Mol. Biol.* **291**, 1169–1179 (1999).
- Pohl, P., Saparov, S. M., Borgnia, M. J. & Agre, P. Highly selective water channel activity measured by voltage clamp: analysis of planar lipid bilayers reconstituted with purified AqpZ. *Proc. Natl Acad. Sci. USA* **98**, 9624–9629 (2001).
- Horner, A. & Pohl, P. Comment on “Enhanced water permeability and tunable ion selectivity in subnanometer carbon nanotube porins”. *Science* **359**, eaap9173 (2018).
- Baaden, M. et al. Biomimetic water channels: general discussion. *Faraday Discuss.* **209**, 205–229 (2018).
- Geise, G. M., Park, H. B., Sagle, A. C., Freeman, B. D. & McGrath, J. E. Water permeability and water/salt selectivity tradeoff in polymers for desalination. *J. Membr. Sci.* **369**, 130–138 (2011).
- Toyoshima, Y. & Thompson, T. E. Chloride flux in bilayer membranes. Chloride permeability in aqueous dispersions of single-walled, bilayer vesicles. *Biochemistry* **14**, 1525–1531 (1975).
- Lang, C. et al. Biomimetic transmembrane channels with high stability and transporting efficiency from helically folded macromolecules. *Angew. Chem. Int. Ed.* **55**, 9723–9727 (2016).
- Taylor, G. J., Venkatesan, G. A., Collier, C. P. & Sarles, S. A. Direct in situ measurement of specific capacitance, monolayer tension, and bilayer tension in a droplet interface bilayer. *Soft Matter* **11**, 7592–7605 (2015).
- Najem, J. S. et al. Memristive ion channel-doped biomembranes as synaptic mimics. *ACS Nano* **12**, 4702–4711 (2018).
- Venkatesan, G. A. et al. Adsorption kinetics dictate monolayer self-assembly for both lipid-in and lipid-out approaches to droplet interface bilayer formation. *Langmuir* **31**, 12883–12893 (2015).
- Taylor, G. J. & Sarles, S. A. Heating-enabled formation of droplet interface bilayers using *Escherichia coli* total lipid extract. *Langmuir* **31**, 325–337 (2015).
- Najem, J. S. et al. Dynamical nonlinear memory capacitance in biomimetic membranes. *Nat. Commun.* **10**, 3239 (2019).
- Werber, J. R. & Elimelech, M. Permselectivity limits of biomimetic desalination membranes. *Sci. Adv.* **4**, eaar8266 (2018).
- Erbakan, M. et al. Molecular cloning, overexpression and characterization of a novel water channel protein from *Rhodobacter sphaeroides*. *PLoS ONE* **9**, e86830 (2014).
- Chowdhury, R. et al. PoreDesigner for tuning solute selectivity in a robust and highly permeable outer membrane pore. *Nat. Commun.* **9**, 3661 (2018).
- Chowdhury, R., Allan, M. F. & Maranas, C. D. OptMAVEN-2.0: De novo design of variable antibody regions against targeted antigen epitopes. *Antibodies* **7**, 23.
- Horner, A. & Pohl, P. Single-file transport of water through membrane channels. *Faraday Discuss.* **209**, 9–33 (2018).

**Publisher's note** Springer Nature remains neutral with regard to jurisdictional claims in published maps and institutional affiliations.

© The Author(s), under exclusive licence to Springer Nature Limited 2019

## Methods

**PAH[4] reconstitution into lipid vesicles.** Both control lipid and PAH[4]-reconstituted lipid vesicular membranes were prepared by the film rehydration method<sup>38</sup>. A PC and PS lipid mixture (3 mg in total) with a molar ratio of 4:1 (mol mol<sup>-1</sup>) was dissolved in chloroform. The required amounts of PAH[4]s, depending on the desired mCLRs, were calculated and dissolved in lipid chloroform solutions. The solutions were transferred into 50 ml round-bottomed flasks and gently dried using a rotary evaporator to form lipid films on the bottom of the flasks. Any residual solvent (chloroform) was removed by placing the flasks in a high vacuum chamber for 16 h. Completely dried films were rehydrated with 1 ml of rehydration buffer (10 mM HEPES, 100 mM NaCl and 0.01% (w/v) NaN<sub>3</sub> at pH 7.0) and extruded 15 times through 0.2 μm polycarbonate track-etched membranes to obtain uniformly sized lipid vesicles ~200 nm in diameter, which was confirmed by a Zetasizer Nano-ZS90 (Malvern Panalytical).

**Water permeability measurement of vesicular membranes.** The osmotic water permeabilities ( $P_f$  (m s<sup>-1</sup>) of lipid vesicular membranes were measured using a SF-300X stopped-flow instrument (KinTek). The vesicles were abruptly exposed to a hypertonic solution (10 mM HEPES, 100 mM NaCl, 100 mM poly(ethylene glycol)<sub>600</sub> and 0.01% (w/v) NaN<sub>3</sub> at pH 7.0) by mixing in the stopped-flow cell to impose an outwardly directed osmotic pressure across the vesicular membranes, and the membrane permeabilities were calculated based on the amount of water efflux from the vesicles driven by the osmotic gradient (shrinking mode of vesicles) (Supplementary Fig. 6). The size change of the vesicles due to the water efflux was monitored through the side-scattering (detection angle of 90° against an incident light of 600 nm wavelength) intensity change with less than 10 ms of dead time after mixing to obtain accurate kinetic information<sup>39</sup>. The kinetic coefficients ( $k$ ) of the size change of vesicles were obtained by fitting the scattering traces into double-exponential functions and used to calculate the osmotic permeability ( $P_f$  (m s<sup>-1</sup>) of vesicular membranes (Supplementary Fig. 7), using equation (1)<sup>21</sup>:

$$P_f = \frac{k}{(S/V_0) \times v_w \times \Delta C_{\text{osm}}} \quad (1)$$

where  $k$  is a larger exponential coefficient of fitted double-exponential function,  $S$  is the initial surface area of the vesicles,  $V_0$  is the initial volume of the vesicles,  $v_w$  is the molar volume of water and  $\Delta C_{\text{osm}}$  is the imposed difference of osmolarity across the vesicular membranes. Note that, for single-channel permeability measurements from mCLR 0.00001 vesicles, a smaller exponential coefficient ( $k$ ) of the fitted double-exponential function was used, because no apparent permeability increase was seen between the control vesicles and the mCLR 0.00001 vesicles from the first exponent. This approach was previously demonstrated and used to characterize water channels that have a low water permeability<sup>13,40</sup>. Accurate  $\Delta C_{\text{osm}}$  values were measured using a freezing point osmometer (Model 3300, Advanced Instruments) for all the tested solutions.

**FCS to evaluate the single PAH[4] channel water permeability.** To calculate the single PAH[4] channel permeability, the actual number of PAH[4]s embedded in reconstituted lipid vesicles was counted using FCS. For the FCS analysis, PAH[4]s were first labelled with 5-(and-6-)-((N-(5-aminopentyl)amino)carbonyl) tetramethylrhodamine (Invitrogen) dyes using dicyclohexylcarbodiimide chemical cross-linkers (Thermo Fisher Scientific). A molar ratio of 1:8:8 of PAH[4]s, dyes and dicyclohexylcarbodiimides were dissolved in dimethyl sulfoxide (DMSO) and reacted for 16 h by stirring at room temperature. Unreacted dyes were removed via dialysis using a Slide-A-Lyzer MINI device (Thermo Fisher Scientific) for 5 d, changing fresh DMSO every 12 h. After the free dye removal by dialysis, labelled PAH[4] channels were harvested by fully evaporating the DMSO solvent inside a high-vacuum chamber for 2 d, and used for both the FCS and FRAP experiments. Dye-labelled PAH[4]s were reconstituted into lipid vesicles using a film rehydration method and the reconstituted vesicles were subsequently subjected to FCS analysis. The fluorescence intensity fluctuation of vesicles ( $\delta F(t)$ ) in a small confocal volume was monitored using a confocal microscope equipped with a time-resolved single-photon counting module (Becker-Hickl GmbH) and the autocorrelation function ( $G(t)$ ) was obtained based on equation (2):

$$G(\tau) = \frac{\langle \delta F(t) \delta F(t + \tau) \rangle}{\langle F(t)^2 \rangle} \quad (2)$$

where  $t$  is time and  $\tau$  is the time lag.  $G(\tau)$  is specifically related to several parameters, as in equation (3):

$$G(\tau) = \frac{1}{N} \sum_{i=1}^M f_i \left[ \frac{1}{1 + \tau/\tau_{\text{Di}}} \right] \left[ \frac{1}{1 + (r/z)^2 (\tau/\tau_{\text{Di}})} \right]^{1/2} \quad (3)$$

where  $r$  and  $z$  are the radius and half height of the confocal volume,  $\tau_{\text{Di}}$  is the lateral diffusion time of fluorescence species  $i$  and  $N$  is the total number of fluorescent species in a confocal volume, which is the number of reconstituted vesicles ( $N_{\text{ves}}$ ) in this case.  $N_{\text{ves}}$  can be simply obtained from the  $y$ -axis intercept of the autocorrelation function ( $G(0) = 1/N_{\text{ves}}$ ). After that, the vesicles were completely

micellized by adding 10% (w/v) of non-ionic detergent octyl β-D-glucoside and the number of channels ( $N_{\text{chan}}$ ) were obtained using same procedure for  $N_{\text{ves}}$  (Supplementary Figs. 8 and 9). The average number of channels per vesicle ( $N_{\text{chan}}/N_{\text{ves}}$ ) was used to calculate both the channel densities in the lipid membranes and the single-channel PAH[4] permeability.

**AFM imaging of PAH[4] clusters in supported bilayer membranes.** AFM analyses were performed to observe the PAH[4] channel clusters in lipid bilayer membranes. Control and PAH[4]-reconstituted (mCLR 0.005) PC/PS vesicles were prepared as described above with an additional buffer composition of 3 mM CaCl<sub>2</sub>. Supported bilayer membranes were prepared by rupturing vesicles (suspending diluted vesicle solutions) on freshly cleaved mica. After 1.5 h of incubation, the membranes were gently washed with water and subjected to AFM imaging in liquid (water) on a Bruker BioScope Resolve AFM. These liquid AFM measurements were conducted in the PeakForce tapping mode using a ScanAsyst Fluid plus tip with a spring constant of 0.7 N m<sup>-1</sup>. The force used for both the control and PAH[4] channel samples was 750 pN or less, and the images contained a minimum of 384 pixels per line. The acquired images were plane-fit to the first order to account for the sample tilt. Multiple line scans were utilized throughout the scan that contained PAH[4] channels to determine the size of their domains. For PAH[4]-reconstituted membranes, island domains ~30 nm in diameter (in the adhesion mode) were identified as spreading over the entire membrane, which was not seen in the control lipid membranes (Supplementary Fig. 12).

**FRAP analysis to observe lateral diffusion of PAH[4]s in lipid bilayer membranes.**

Two PC/PS vesicles were prepared; one was PC/PS vesicles with dye-labelled PAH[4]s (mCLR 0.005) and the other (control vesicle) was PC/PS with PAH[4]s (unlabelled, mCLR 0.005) and an additional 0.5 mol% of Texas Red 1,2-dihexadecanoly-sn-glycero-3-phosphoethanolamine (TR-DHPE) lipids. TR-DHPE-containing control vesicles were used to confirm the bilayer formation and obtain the membrane viscosity, as described below. The vesicle solutions were combined with a buffer solution to create a vesicle environment with a final concentration of 2 mM CaCl<sub>2</sub>, 100 mM NaCl and 10 mM HEPES at pH 7. Supported bilayers were made by rupturing the vesicles on a cleaned glass coverslip in a polydimethylsiloxane well. After a fusion time of 10 min, the formed bilayers were rinsed with buffer (100 mM NaCl and 10 mM HEPES at pH 7.0), scratched with tweezers to remove a small section of bilayer and rinsed with the same buffer a second time. The FRAP experiments were conducted on a Nikon Eclipse TE-2000-U inverted microscope through a ×10 objective lens. A 532 nm laser (Spectra Physics) was used to bleach the labelled channel or the TR-DHPE. The bleach spot diameter was approximately 16 μm. The fluorescence intensity was monitored every 3 s for the initial 75 s, and then every 30 s for the remainder of the experiments (Supplementary Fig. 13). The fluorescent recovery curves were used to determine the diffusion coefficients of the labelled PAH[4] channel and TR-DHPE, respectively. The fluorescence intensity of the bleached spot at a given time was divided by the intensity of a non-bleached region to correct for differences in light intensity and photobleaching. The normalized fluorescence recovery,  $f(t)$ , was calculated using equation (4):

$$f(t) = \frac{I_t - I_0}{I_i - I_0} \quad (4)$$

where  $I_t$  is the normalized spot intensity at time  $t$ ,  $I_0$  is the normalized spot intensity immediately after bleaching and  $I_i$  is the average spot intensity prior to bleaching.

The recovery as a function of time was fit to an exponential equation to obtain the mobile fraction,  $A$ , as well as the time of half recovery,  $\tau_{1/2}$ , shown in equations (5) and (6):

$$f(t) = A(1 - e^{-t/\tau}) \quad (5)$$

$$\tau_{1/2} = \frac{\ln 2}{\tau} \quad (6)$$

The lateral diffusion coefficient,  $D_{\text{lat}}$ , was calculated using equation (7), where  $\omega$  is the half-width of the Gaussian laser beam:

$$D_{\text{lat}} = \frac{0.88 \times \omega^2}{4 \times \tau_{1/2}} \quad (7)$$

**Measurement of activation energy of water permeation through PAH[4] channels.** Water permeability measurements of both the control and channel-reconstituted lipid membranes were repeated at different temperatures (between 5 and 25 °C) to measure the activation energy ( $E_a$ ) of water permeation through the channels as well as the lipid membrane matrix (Supplementary Fig. 14). Measurements were performed under the swelling mode for this part of the study. Channel-mediated water permeabilities at each temperature were obtained by subtracting the control lipid membranes' permeability from the channel-reconstituted membranes' permeability. Water permeability ( $P_f$  (μm s<sup>-1</sup>)) and the  $E_a$  of water permeation is related by the Arrhenius equation<sup>14,22,23</sup>:

$$P_f = A e^{-E_a/RT} \quad (8)$$

where  $A$  is a pre-exponential constant,  $R$  is the ideal gas constant and  $T$  is the temperature (K).  $E_a$  can simply be extracted from a slope of the Arrhenius plot, as shown in equation (9) (Fig. 2d):

$$\ln P_f = \ln A - \frac{E_a}{R} \frac{1}{T} \quad (9)$$

**Cl<sup>-</sup> ion permeability measurement.** Measurements of the Cl<sup>-</sup> permeability of both the control and PAH[4]-reconstituted lipid vesicular membranes were performed using stopped-flow fluorescence experiments. Among several halide ion sensitive colloidal quenching dyes, lucigenin dyes were selected as the measurement probes as they have the highest Stern–Volmer constant value among commercial dyes ( $K_{SV} = 390 \text{ M}^{-1}$  for chloride ions in aqueous solutions) and, therefore, the highest sensitivity to a Cl<sup>-</sup> concentration change<sup>41</sup>. To measure accurately the Cl<sup>-</sup> influx into vesicular membranes, the  $K_{SV}$  of lucigenin inside ~200 nm PC/PS vesicles was first determined ( $95 \text{ M}^{-1}$  for intravesicular environments (Supplementary Fig. 15)). The excitation wavelength was set as 455 nm using a monochromator and photomultiplier tube (PMT) module was equipped with a BrightLine fluorescence 534/30 emission filter. Lucigenin-encapsulating vesicles prepared with a Cl<sup>-</sup> free buffer (10 mM HEPES, 100 mM KNO<sub>3</sub>, 10 μM valinomycin and 0.01% (w/v) Na<sub>2</sub>S<sub>2</sub>O<sub>8</sub> at pH 7.0) were abruptly exposed to different Cl<sup>-</sup> gradients in the stopped-flow measurement cell (for example, to impose a 20 mM Cl<sup>-</sup> gradient, the same volumetric amount of Cl<sup>-</sup>-containing buffer (10 mM HEPES, 40 mM KCl, 60 mM KNO<sub>3</sub>, 10 μM valinomycin and 0.01% (w/v) Na<sub>2</sub>S<sub>2</sub>O<sub>8</sub> at pH 7.0) as that of the vesicle solution was mixed in the measurement cell) and the fluorescence intensity change was monitored. Note that potassium ionophore valinomycin was added to the vesicles beforehand to mitigate charge imbalance across the membrane, and therefore prevent an underestimation of the Cl<sup>-</sup> permeability if an electrical potential developed as a consequence. The initial fluorescence kinetic information ( $dF/F|_{t=0}$ ) is quite important for an accurate evaluation of the Cl<sup>-</sup> permeability and stopped-flow traces (Supplementary Fig. 16). More than ten traces of fluorescence intensity change were recorded for each measurement and the averaged trace was used for the analysis. The vesicular membrane mole flux of Cl<sup>-</sup> ions ( $j_{Cl}$ ) at each tested Cl<sup>-</sup> concentration condition was calculated using equation (10):

$$j_{Cl} = \frac{d[\text{mole}]}{S \times dt} = \frac{V}{S} \frac{d[\text{Cl}^-]}{dt} \Big|_{t=0} = \frac{-V}{S \times K_{SV} \times F_0} \frac{dF}{dt} \Big|_{t=0} \quad (10)$$

where  $S$  and  $V$  are the surface area and volume of the vesicles,  $[\text{Cl}^-]$  is molar concentration of Cl<sup>-</sup> ions inside vesicles,  $K_{SV}$  is the determined Stern–Volmer constant of the lucigenin dyes inside the vesicles (~95 M<sup>-1</sup>),  $F_0$  is the fluorescence intensity under Cl<sup>-</sup>-free conditions (fluorescence intensity at  $t=0$ ). The Cl<sup>-</sup> permeability coefficient ( $B_{Cl}$  (cm s<sup>-1</sup>)) of the membranes was obtained from slope of the  $j_{Cl}$  plot as a function of the Cl<sup>-</sup> concentration gradients using equation (11) (Fig. 2f):

$$B_{Cl} = \frac{dj_{Cl}}{d[\text{Cl}^-]} \quad (11)$$

The single PAH[4] channel Cl<sup>-</sup> permeability coefficient ( $B_{Cl,PAH}$  (cm<sup>3</sup> s<sup>-1</sup>)) was calculated based on the channel density in the lipid membranes obtained from the FCS analyses (equation (12)):

$$B_{Cl,PAH} = \frac{d(j_{Cl,PAH,lipid} - j_{Cl,lipid})}{d[\text{Cl}^-]} \times \frac{1}{\sigma_{PAH}} \quad (12)$$

where  $j_{Cl,PAH,lipid}$  is the PAH-reconstituted membrane Cl<sup>-</sup> mole flux,  $j_{Cl,lipid}$  is the bare lipid membrane Cl<sup>-</sup> mole flux and  $\sigma_{PAH}$  is the number of PAH[4] channels per unit membrane area.

**Current-to-voltage measurement of PAH[4]-reconstituted lipid membranes using the DIB system.** A DIB set-up was used to characterize the ionic transport properties of PAH[4] and PAP[5] channels (as a control) in lipid bilayer membranes. The lipid membranes were formed between two aqueous droplets anchored to wire-type electrodes in a transparent reservoir filled with oil, as described elsewhere<sup>28,29</sup>. In brief, the set-up consisted of two lipid-encased aqueous droplets that hung from Ag/AgCl wires (Goodfellow) in oil (1:2 mixture of hexadecane (≥99%, Sigma) and decane (≥95%, Sigma)). When the droplets were brought into contact, the lipid tails from each droplet interacted with each other at the interface to expel oil and form an oil-depleted hydrophobic centre (that is, a thinned lipid bilayer). To help the droplets anchor to the Ag/AgCl wires, we coated their ball-ended tips with a 1% agarose gel solution. To confirm the lipid bilayer formation, which is reflected as an increase in membrane capacitance, we supplied a 10 Hz, 10 mV triangular wave to the electrodes using a function generator (Hewlett-Packard 3314A). Owing to the capacitive nature of the membrane, the resulting current response was square-like. As the area of the thinned lipid membrane grew, the peak-to-peak current amplitude increased until it reached a steady state. To generate the  $I$ - $V$  relationships, we applied a 0.01 Hz, 50 mV sinusoidal voltage waveform and recorded the induced current. In parallel, to monitor the changes in the membrane we acquired images of the droplets from

below through a ×4 objective lens of an Olympus IX51 inverted microscope using a QI Click charge-coupled device. All the current recordings were made using an Axopatch 200B patch clamp amplifier and Digidata 1440 data acquisition system (Molecular Devices). For all the measurements, the droplets and measurement probes were placed under a lab-made Faraday cage to minimize noise from the environment.

**MD simulations.** All atom MD simulations were performed using the MD program NAMD2<sup>42</sup>. PAH[4] channels (25) were arranged in a 5 × 5 array and embedded into a 14.4 × 14.4 nm<sup>2</sup> patch of a pre-equilibrated POPC (1-palmitoyl-oleoyl-sn-glycerophosphocholine) lipid bilayer membrane. The lipid patch was generated from the CHARMM-GUI membrane builder<sup>43</sup> and equilibrated for approximately 400 ns. Lipid molecules that overlapped with the channels were removed. The system was then solvated with the water<sup>44</sup> using the Solvate plugin of VMD. Sodium and chloride ions were added using the Autoionize plugin of VMD to produce an electrically neutral solution of 0.6 M salt concentration. The resulting system measured 14.4 × 14.4 × 10 nm<sup>3</sup> and contained approximately 170,000 atoms. Next, we created three conformations of PAH[4] dimers, namely lateral, orthogonal and inverted, each of which comprised two units of single PAH[4] channels (Supplementary Information gives details). We embedded 25 PAH[4] dimers in a regular 5 × 5 array into a 20 × 20 nm<sup>2</sup> patch of a pre-equilibrated POPC lipid bilayer membrane. We solvated the structure and added ions to create a charge-neutral 0.6 M solution of NaCl in each system. The resulting system measured 20 × 20 × 10 nm<sup>3</sup> and contained approximately 353,000 atoms. We created four such systems, three of which contained dimer arrays with different conformations and one in which the water molecules were placed inside an array of orthogonal PAH[4] dimers. Choosing the most conductive dimer conformation from these simulations, we created a pre-assembled cluster structures using the self-docking protocol developed in OptMAVEN-2.0<sup>46</sup>. Three different thermodynamically stable conformations of PAH[4] clusters were generated and embedded into a 14.4 × 14.4 nm<sup>2</sup> patch of a pre-equilibrated POPC lipid bilayer membrane. Each structure was solvated by a 0.6 M NaCl solution. Each system measured 14.4 × 14.4 × 10 nm<sup>3</sup> and contained approximately 172,000 atoms.

The assembled systems were subjected to energy minimization using the conjugate gradient method that removed steric clashes between the solute and solvent atoms. After the energy minimization, the systems were subjected to a short equilibration at a constant number of atoms ( $N$ ), constant pressure ( $P = 1$  bar) and constant temperature ( $T = 303$  K). This was an NPT ensemble with harmonic restraints on all the non-hydrogen atoms of PAH[4] channels with respect to their initial positions (with spring constants of 1 kcal mol<sup>-1</sup> Å<sup>-2</sup>). Subsequently, the harmonic restraints were released completely, and the system was equilibrated free of any restraints.

The initial all-atom configuration of the AQP1 system was built starting from the all-atom structure of bovine AQP1, Protein Data Bank entry 1j4n<sup>17</sup>. The structure was embedded into a POPE (1-palmitoyl-2-oleoyl-sn-glycero-3-phosphoethanolamine) lipid bilayer membrane as described in our previous study<sup>45</sup>. For the sake of comparison, the AQP1 system was simulated using exactly the same simulation protocols as for the PAH[4] systems with a 200 ns simulation time.

All the MD simulations were performed using periodic boundary conditions and the particle mesh Ewald method to calculate the long-range electrostatic interactions in NAMD2<sup>42</sup>. A Nose–Hoover Langevin piston<sup>46,47</sup> and Langevin thermostat were used to maintain a constant pressure and temperature in the system<sup>48</sup>. CHARMM36 force-field parameters<sup>49,50</sup> described the bonded and non-bonded interactions among the PAH[4] channels, lipid bilayer membranes, water and ions along with NBFIX corrections for non-bonded interactions<sup>51,52</sup>. A 8–10–12 Å cutoff scheme was used to calculate van der Waals and short-range electrostatics forces. All the simulations were performed using 1 fs time steps to integrate the equation of motion. The SETTLE algorithm<sup>53</sup> was applied to keep the water molecules rigid, whereas the RATTLE algorithm<sup>54</sup> constrained all other covalent bonds that involved hydrogen atoms. For each system, 300–400 ns equilibrium MD simulations were performed, which gave rise to transmembrane water permeation through irregular dendritic paths between the PAH[4] structures. The coordinates of the system were saved at the interval of a 4.8 ps simulation. The analysis and post-processing the simulation trajectories were performed using VMD and CPPTRAJ<sup>55</sup>.

## Data availability

The datasets that support the finding of this study are available in ScholarSphere repository with the identifier(s) (<https://doi.org/10.26207/ykbn-r806>).

## References

- Woodle, M. C. & Papahadjopoulos, D. [9] Liposome preparation and size characterization. *Methods Enzymol.* **171**, 193–217 (1989).
- Latimer, P. & Pyle, B. E. Light scattering at various angles: theoretical predictions of the effects of particle volume changes. *Biophys. J.* **12**, 764–773 (1972).
- Tong, J., Canty, J. T., Briggs, M. M. & McIntosh, T. J. The water permeability of lens aquaporin-0 depends on its lipid bilayer environment. *Exp. Eye Res.* **113**, 32–40 (2013).

41. Biwersi, J., Tulk, B. & Verkman, A. S. Long-Wavelength chloride-sensitive fluorescent indicators. *Anal. Biochem.* **219**, 139–143 (1994).
42. Phillips, J. C. et al. Scalable molecular dynamics with NAMD. *J. Comput. Chem.* **26**, 1781–1802 (2005).
43. Jo, S., Kim, T., Iyer, V. G. & Im, W. CHARMM-GUI: a web-based graphical user interface for CHARMM. *J. Comput. Chem.* **29**, 1859–1865 (2008).
44. Jorgensen, W. L., Chandrasekhar, J., Madura, J. D., Impey, R. W. & Klein, M. L. Comparison of simple potential function for simulating liquid water. *J. Chem. Phys.* **79**, 926–935 (1983).
45. Decker, K. et al. Selective permeability of truncated aquaporin 1 in silico. *ACS Biomater. Sci. Eng.* **3**, 342–348 (2017).
46. Feller, S. E., Zhang, Y., Pastor, R. W. & Brooks, B. R. Constant pressure molecular dynamics simulation: the Langevin piston method. *J. Chem. Phys.* **103**, 4613–4621 (1995).
47. Martyna, G. J., Tobias, D. J. & Klein, M. L. Constant pressure molecular dynamics algorithms. *J. Chem. Phys.* **101**, 4177–4189 (1994).
48. Sindhikara, D. J., Kim, S., Voter, A. F. & Roitberg, A. E. Bad seeds sprout perilous dynamics: stochastic thermostat induced trajectory synchronization in biomolecules. *J. Chem. Theory Comput.* **5**, 1624–1631 (2009).
49. Best, R. B. et al. Optimization of the additive CHARMM all-atom protein force field targeting improved sampling of the backbone  $\phi$ ,  $\psi$  and side-chain  $\chi_1$  and  $\chi_2$  dihedral angles. *J. Chem. Theory Comput.* **8**, 3257–3273 (2012).
50. Klauda, J. B. et al. Update of the CHARMM all-atom additive force field for lipids: validation on six lipid types. *J. Phys. Chem. B* **114**, 7830–7843 (2010).
51. Yoo, J. & Aksimentiev, A. New tricks for old dogs: improving the accuracy of biomolecular force fields by pair-specific corrections to non-bonded interactions. *Phys. Chem. Chem. Phys.* **20**, 8432–8449 (2018).
52. Yoo, J. & Aksimentiev, A. Improved parametrization of  $\text{Li}^+$ ,  $\text{Na}^+$ ,  $\text{K}^+$ , and  $\text{Mg}^{2+}$  ions for all-atom molecular dynamics simulations of nucleic acid systems. *J. Phys Chem Lett* **3**, 45–50 (2011).
53. Miyamoto, S. & Kollman, P. A. SETTLE: an analytical version of the SHAKE and RATTLE algorithm for rigid water models. *J. Comput. Chem.* **13**, 952–962 (1992).
54. Andersen, H. C. RATTLE: a 'velocity' version of the SHAKE algorithm for molecular dynamics calculations. *J. Comput. Phys.* **52**, 24–34 (1983).
55. Humphrey, W., Dalke, A. & Schulten, K. VMD: visual molecular dynamics. *J. Mol. Graph. Model* **14**, 33–38 (1996).

### Acknowledgements

The authors acknowledge financial support from the National Science Foundation (NSF) CAREER grant (CBET-1552571) to M.K. for this work. A.A. and H.J. acknowledge support from the National Science Foundation under grant DMR-1827346 and the National Institutes of Health under grant P41-GM104601. Additional support was provided by NSF grant CBET-1804836 to M.K. Supercomputer time was provided through XSEDE Allocation Grant no. MCA05S028 and the Blue Waters petascale supercomputer system at the University of Illinois at Urbana–Champaign. H.J. acknowledges the Government of India for the DST-Overseas Visiting Fellowship in Nano Science and Technology.

### Author contributions

W.S., H.J., A.A. and M.K. conceived and designed the research. W.S. and Y.-x.S. performed the experiments with the assistance of J.S.N., C.L., C.B.H., Y.-M.T., M.F., M.E.P. and J.-I.H. in specialized analytical tools. H.J. and R.C. performed the computer simulations. W.S., H.J., R.C., C.D.M., P.S.C., R.J.H., S.A.S., J.-I.H., A.A. and M.K. analysed the data. W.S., H.J., R.C., A.A. and M.K. co-wrote the paper.

### Competing interests

The authors declare no competing interests.

### Additional information

**Supplementary information** is available for this paper at <https://doi.org/10.1038/s41565-019-0586-8>.

**Correspondence and requests for materials** should be addressed to M.K.

**Peer review information** *Nature Nanotechnology* thanks Andreas Horner, Meni Wanunu and the other, anonymous, reviewer(s) for their contribution to the peer review of this work.

**Reprints and permissions information** is available at [www.nature.com/reprints](http://www.nature.com/reprints).